Earth Sci Inform (2017) 10:287–301
DOI 10.1007/s12145-017-0291-9

RESEARCH ARTICLE

Unmanned aerial vehicle based remote sensing method for monitoring a steep mountainous slope in the Three Gorges Reservoir, China

Haifeng Huang[1,2,3] · **Jingjing Long**[1,3] · **Haiyu Lin**[1,3] · **Lei Zhang**[1,3] · **Wu Yi**[3,4] · **Bangjun Lei**[2]

Received: 31 March 2016 / Accepted: 24 January 2017 / Published online: 8 February 2017
© Springer-Verlag Berlin Heidelberg 2017

Abstract Monitoring has been considered to be the most effective means of preventing and mitigating geo-hazards. Unmanned aerial vehicle (UAV) based remote sensing has been proven to be a viable method for monitoring relatively flat areas, but has typically encountered challenges on steep mountainous slopes. The Qinglingou Slope, which is located at the head of the Three Gorges Reservoir, China, was selected as a case study, and a UAV-based remote sensing method was applied to monitor this steep mountainous slope. The UAV, which was equipped with a camera, was used to acquire images on May 10 and Sept. 13, 2015. At the same time, a plan for establishing and measuring a detailed network of ground control points (GCPs) and check points was carefully designed and implemented, according to the local conditions. Georeferenced digital surface models (DSMs) and digital orthophotos were obtained by photogrammetric processing. Based on the results, a simple and quick method that identified and quantified slope deformation by calculating and analyzing the changes in the DSMs was developed. The results showed that the UAV-based remote sensing method was rapid, safe and effective, and it could be valuable for monitoring a large number of steep mountainous slopes in the Three Gorges Reservoir.

Keywords Unmanned aerial vehicle (UAV) · Remote sensing · Slope monitoring · Digital surface model (DSM) · Digital orthophoto · Volume change

Communicated by: H. A. Babaie

✉ Haifeng Huang
hhf@ctgu.edu.cn

[1] Key Laboratory of Disaster Prevention and Mitigation of Hubei Province, China Three Gorges University, No. 8 Univ. Ave, Yichang, People's Republic of China 443002

[2] Hubei Key Laboratory of Intelligent Vision Based Monitoring for Hydroelectric Engineering, China Three Gorges University, No. 8 Univ. Ave, Yichang, People's Republic of China 443002

[3] National Field Observation and Research Station of Landslides in the Three Gorges Reservoir Area of Yangtze River, China Three Gorges University, No. 8 Univ. Ave, Yichang, People's Republic of China 443002

[4] Collaborative Innovation Center for Geo-Hazards and Eco-Environment in the Three Gorges Area, Hubei Province, No. 8 Univ. Ave, Yichang, People's Republic of China 443002

Introduction

The Three Gorges area lies in the transition zone between eastern and western China, where the geography becomes mountainous. When the Three Gorges Project was completed, the reservoir water level rose approximately 100 m (Huang et al. 2014a), inundating all flat lowlands. Accordingly, steeper slopes were distributed along the river banks. Moreover, a great deal of construction, such as new towns, factories, wharves, public roads, etc. had to be carried out on the slopes along the river banks. Thus, bulk excavation was usually unavoidable. Excavation increased the slopes, which were already high. Moreover, new slopes were excavated, forming many steep mountainous slopes in the Three Gorges Reservoir, and the average gradient of these slopes was at least 40° (Yin 1998). As a result, these slopes are prone to deformation and give rise to geo-hazards such as landslides, rockfalls, etc. because of their steep gradients, coupled with the impacts of rainfall, reservoir water fluctuations, and human activities (Jian et al. 2014; Huang et al. 2015). Therefore, prevention and control the deformation of these steep mountainous slopes has become an important aspect of geo-hazards risk management in the Three Gorges Reservoir.

Monitoring has been considered to be the most effective means of preventing and mitigating geo-hazards (such as landslides, unstable slopes, etc.) (Huang et al. 2014a; b). A wide range of techniques have been used, including Global Navigation Satellite Systems (GNSSs, e.g., GPS and Compass), extensometers, field surveys with cameras, etc. (Malet et al. 2002; Rawat et al. 2011). However, these conventional ground monitoring techniques are difficult to implement on steep mountainous slopes, many of which are inaccessible, and even if they could be reached, this type of monitoring on steep slopes is still time-consuming work that carries great risk. In addition, these point-based monitoring techniques can only collect movement data from a few measurement stations on the slope surface. Therefore, deformation information on the whole surface could not be captured (Kasperski et al. 2010). Subsequently, ground-, airborne- and satellite-based remote sensing techniques began to attract considerable attention (Dewitte et al. 2008; Joyce et al. 2009; Kasperski et al. 2010; Booth et al. 2013; Tofani et al. 2013). However, the images acquired with most of these techniques were not of sufficient spatial or temporal resolution for monitoring most slope deformation (Tahar 2012). In addition, these methods involved huge cost, complicated technologies, etc. and in particular were subject to the effects of time and weather conditions (Niethammer et al. 2011).

Unmanned aerial vehicle (UAV) based remote sensing, which is a low-cost alternative for image acquisition with high spatiotemporal resolution, has seen much interest in recent years (Colomina and Molina 2014; Niu et al. 2014). In addition, the development of image processing techniques, especially Structure-from-Motion (SfM), has provided effective and low-cost photogrammetric techniques to obtain high-

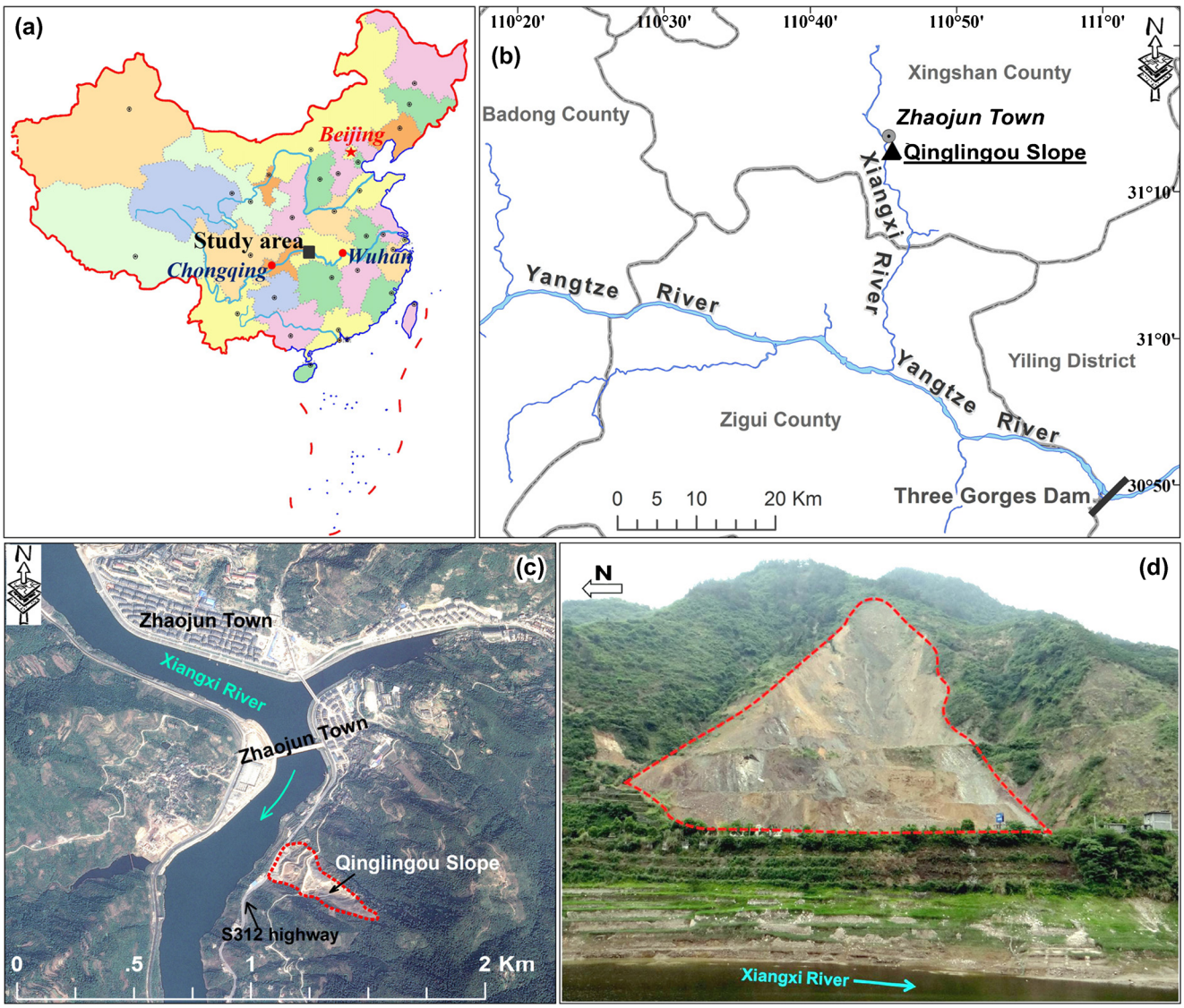

Fig. 1 Location and general view of the study area: **a** location in China, **b** location relative to Three Gorges Reservoir, **c** location of Zhaojun Town, and **d** upward view of the Qinglingou Slope

resolution datasets, has greatly promoted the application of UAV-based remote sensing (Harwin and Lucieer 2012; Westoby et al. 2012; Javernick et al. 2014; Lucieer et al. 2014; Prosdocimi et al. 2015). For example, the UAV-based remote sensing technique began to be used for slope or landslide monitoring. Niethammer et al. studied the Super-Sauze landslide (France) continuously with UAV-based remote sensing (Niethammer et al. 2009; Niethammer et al. 2010; Niethammer et al. 2012; Tahar 2012), including UAV systems, data acquisition, ortho-mosaic and digital terrain model (DTM) generation, movement vectors analysis and DTM comparison. This study led to the conclusion that UAV-based remote sensing could provide an excellent data source to measure changes in landslide structure. Lucieer et al. (2014) and Turner et al. (2015) took the Home Hill landslide (Australia) as an example and described an image-processing workflow based on UAV technology. They also elaborated the Structure-from-Motion technique and used image correlation for detailed monitoring of the landslide. They then used UAVs to collect a time series of images over four years during seven epochs to assess landslide dynamics. The results demonstrated that some image analysis algorithms could map and monitor landslide dynamics with a UAV over a relatively long time series. All these studies showed that using UAV to monitor landslides was a viable method. Whereas the above applications were mainly concerned with relatively flat areas (gradient ≤25°), monitoring steep mountainous slopes (gradient >40°) using UAV-based remote sensing is still challenging, because it is very difficult to carry out any field work on such steep slopes where humans can hardly walk.

The main aim of carrying out this study was to establish a rapid, safe, effective and complete UAV-based remote sensing method, including on-site image acquisition, establishment and measurement of ground control points (GCPs) and check points, image processing, and slope deformation identification and quantification. This method can then serve as a reference for monitoring a large number of steep mountainous slopes near the Three Gorges Reservoir of China. Thus, a steep mountainous slope which was named Qinglingou Slope in Three Gorges Reservoir area was first introduced. Then, a UAV-based remote sensing system, image acquisition process and image processing method were elaborated. Finally, a simple and quick method that identified and quantified slope deformation by calculating and analyzing the changes in the digital surface models (DSMs) was developed.

Study area

The Qinglingou Slope is located at the head of the Three Gorges Reservoir and on the left bank of Xiangxi River, a tributary of the Yangtze River, in Xingshan County, Hubei Province, central China (Fig. 1a, b). The slope area was selected as a site for obtaining rock and soil in 2007. These materials were used as backfill to build the new Zhaojun

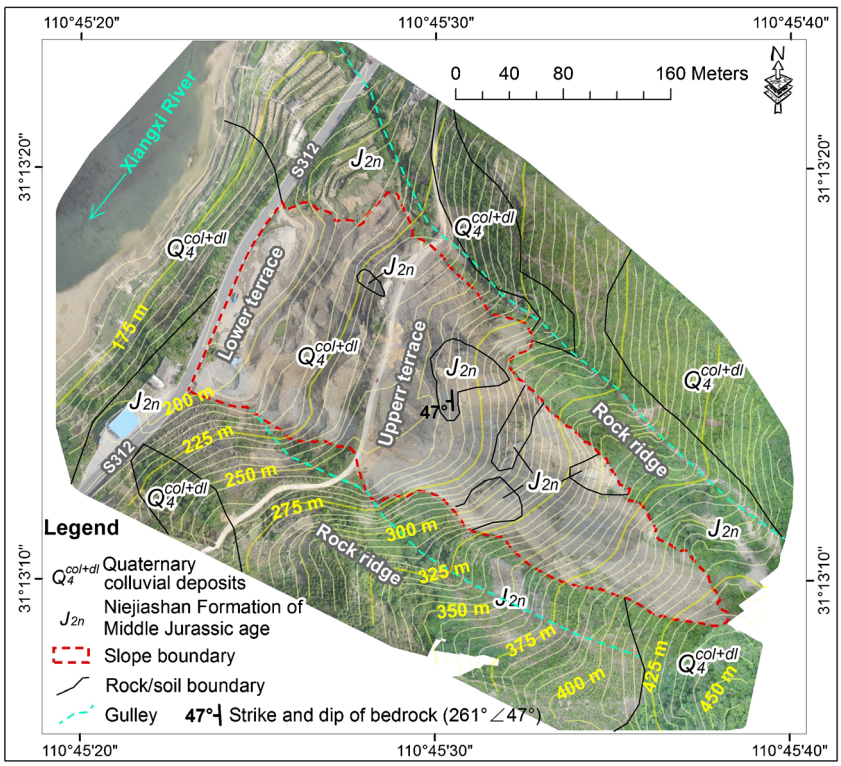

Fig. 2 Simplified geological and topographic map of the Qinglingou Slope. The base map is a digital orthophoto from May 10, 2015. The topographic contours have been simplified

Town (Fig. 1c) before the impoundment of the Three Gorges Reservoir. Therefore, the Qinglingou Slope was originally formed by bulk excavation. A large-scale slide occurred on May 31, 2008. In recent years, sporadic excavation has continued on the lower part, while soil mass and rock debris have collapsed constantly onto the upper part. These processes determine the current condition of Qinglingou Slope (Fig. 1d).

Considering that the slope continuously threatened the safety of a provincial highway (S312) and the new Zhaojun Town (if the whole slope or a large-scale mass slid into the Xiangxi River, large swells would inevitably damage the town), the government wanted to completely control it. Thus, a detailed engineering survey of Qinglingou Slope was carried out in August of 2014. At the same time, a large-scale topographic map (1: 500 scale) was obtained using total station measurements. Fig. 2 shows the simplified results.

Geomorphologically, the slope lies between two gullies, outside of which are bedrock ridges. The boundaries on both sides of the slope extend along two gullies and then gradually close on the upper part. The slope thus has an irregular shape like a long tongue. It has a length of 450 m and a maximum width of 200 m at the toe, a planar area of approximately 53,000 m^2, and a slope direction of 312°. The elevation of the slope ranged from 190 m to 435 m. That is, the difference in elevation was 245 m and the average gradient was 33°. In addition, two terraces exist on the slope. The lower terrace is at the toe of the slope and is located inside of the provincial highway (S312). Its elevation was approximately 195 m. The upper terrace is in the middle of the slope and is located inside of a village-level highway. Its elevation is approximately 245 m. The upper part of this slope, where the elevation is above 245 m, is much steeper. Here, the average gradient reaches 43° and the maximum gradient reaches 70°, which means that humans could hardly stand or climb on the slope.

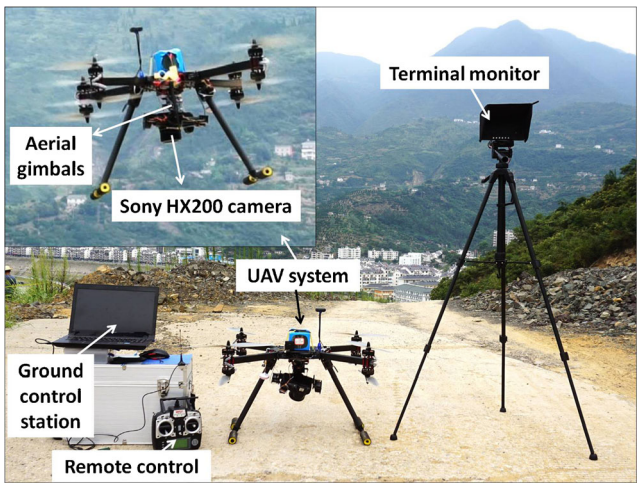

Fig. 3 UAV system fitted with Sony HX200 camera

Lithologically, the bedrock belongs to the Niejiashan Formation of Middle Jurassic Age (J_2n), which consists of feldspathic quartz sandstone and siltstone. The strike and dip of the bedrock is 261°∠47°; that is, the bedrock is inclined in the direction of the topographic slope. The colluvial deposits (Q_4^{col+dl}) consisted of sandy clay and rock debris that originated from the sedimentary rock. The engineering survey showed that the bedrock was mainly found in both ridges. Some local bedrock also outcropped within the slope. The colluvial deposits mainly covered the slope.

In addition, significant differences in texture and color could be easily identified between the inside and outside portions of the slope; lush vegetation covered the outside, while the inside was bare soil and rock.

According to the engineering survey results, it would be difficult to design an economical and effective method to eliminate the geo-hazard completely, especially over the whole slope, because of its large scale and steep gradient. Fortunately, monitoring was carried out at the same time as the engineering survey. The results showed that the slope was stable as a whole; only local deformation (mainly referring to the constant collapse of soil mass and rock debris onto the upper part) occurred. So, regular monitoring was identified as the most effective prevention measure for the Qinglingou Slope.

Given the adaptability, flexibility, cost, and low risk associated with UAV-based remote sensing and the deformation characteristics of the slope, a UAV-based remote sensing system was used to monitor and analyze the slope deformation.

Methods

UAV system

Usually, a complete UAV is composed of a flight platform system and a ground control system (Bürkle et al. 2011; Colomina and Molina 2014). To quickly acquire high spatial resolution photographs of the Qinglingou Slope, a UAV-based remote sensing system was assembled as follows (Fig. 3).

A four-axis, eight-rotor UAV flight platform was assembled. This system featured simple controls, convenient takeoff and landing, and fixed-point hovering. Further advantages of this system included additional power, stability and safety.

A Sony HX200 camera with 18 effective megapixels and a Vario Sonnar T* 4.8–144 mm F/2.8–5.6 lens was used to collect the photographs. The camera was carried on a set of aerial gimbals that attached to the bottom of the UAV. The photo capture rate was controlled by the UAV's flight control board, which could be programmed to emit a trigger pulse at a desired frequency, and the flight control board was connected to a steering engine that triggered the shutter of the camera. To ensure that high quality photos with fine definition and

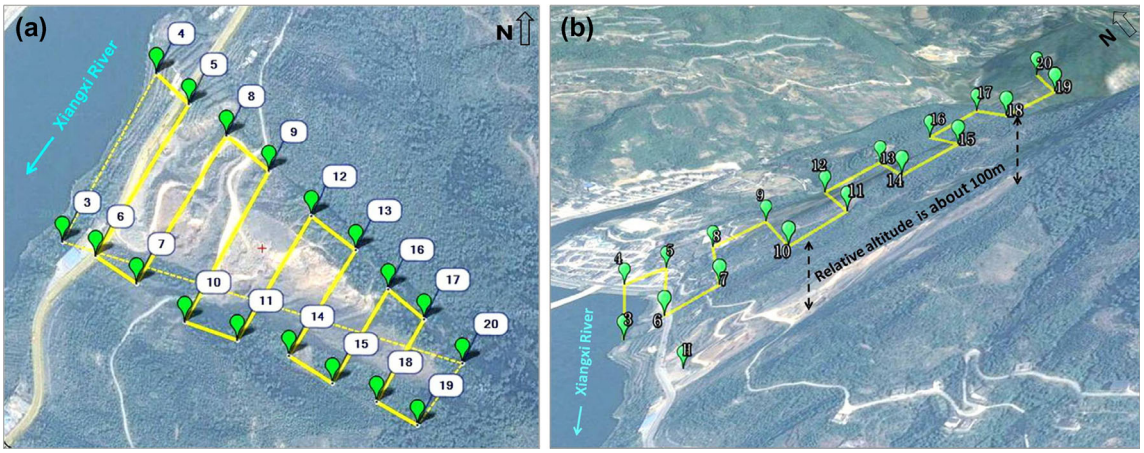

Fig. 4 Preliminary flight plan based on Google Earth: **a** regular grid pattern in plane, **b** flight height changed with slope altitude in vertical

constant lens orientation could be taken during the flight, the use of the aerial gimbals to maintain the stability of the camera was very necessary. The aerial gimbals were also controlled by the flight control board.

The ground control system mainly includes the ground control station, which was a notebook computer that was used to set flight parameters and monitor the flight status. A remote control was used to control the UAV manually in case of emergency. In addition, a terminal monitor was used to show real-time images and the flight parameters of the aircraft.

In a word, the UAV was an autonomous flight system that could fly and take photographs automatically according to a flight plan. In addition, a flight duration of approximately 20 min ensured that sufficient photos of the whole slope surface could be collected at one time.

Image acquisition

Before the first flight on May 10, 2015, a comprehensive flight plan was designed, because such plans are indispensable and vital for flight safety and image acquisition (Santamaria et al. 2012). The flight planning process can be divided into the preliminary flight plan design and on-site verification. The preliminary flight plan was designed using Google Earth. As

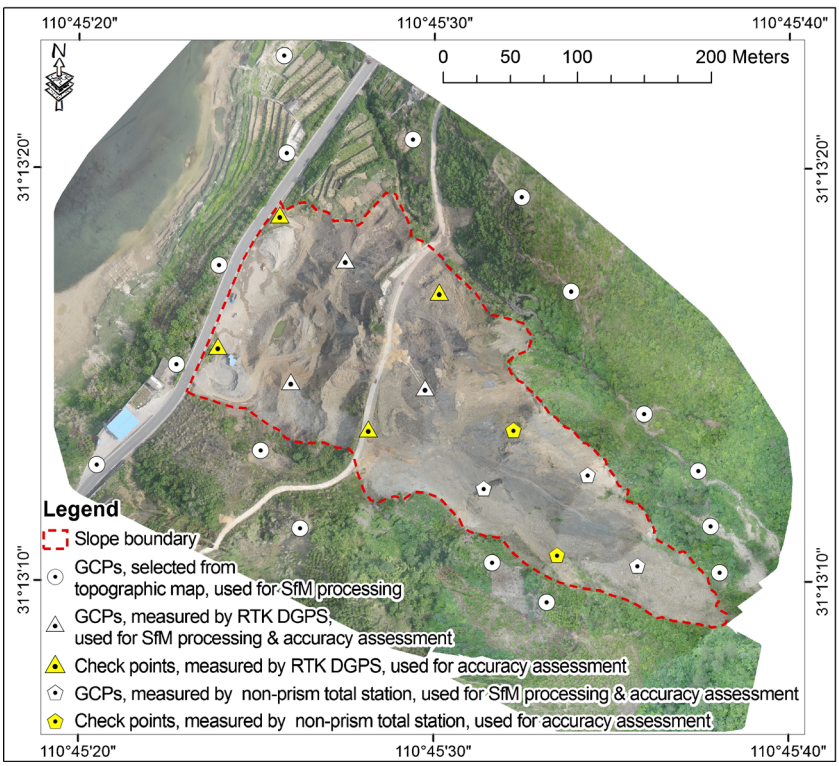

Fig. 5 Network of GCPs and check points established on the Qinglingou Slope. The base map is a digital orthophoto from May 10, 2015

usual, a regular grid pattern laid out in a plane was used (Fig. 4a). It is worth noting that the flight elevation had to change with the altitude of the slope surface to maintain a relatively constant altitude (approximately 100 m) above the ground (Fig. 4b) in order to get clear photos with a Ground Sampling Distance (GSD) of less than 5 cm/pixel. On-site flight plan verification was indispensable because location errors usually exist in Google Earth, especially in mountainous regions, where the planar location errors could reach several tens of meters or even up to a hundred meters, and altitude errors could also reach dozens of meters. Thus, the flight plan was relocated according to the actual, on-site location data that came from the UAV's GPS unit to ensure that the flight was safe and just covered the whole slope area. In addition, based on the expected GSD, flight altitude, 80% frontal overlap and 70% side overlap between photos, the flight plan software could generate routes automatically. Of course, the final flight plan had to be entered into the flight control module of the UAV. In addition, the flight speed was set to 10 m/s and the time interval at which photos were taken was set to 1.5 s. That is, one photo was taken every 15 m. After the first successful flight and image acquisition on the Qinglingou Slope, the flight plan data were saved to a text file, which was also used for the second flight on Sept. 13, 2015.

In order to increase and check the absolute accuracy of the results, the establishment and measuring of GCPs and check points were very important (Niethammer et al. 2012; Lucieer et al. 2014; Niu et al. 2014). However, this process presented important challenges on the Qinglingou Slope, because the steep upper portion and the lush vegetation on the outside of the slope seriously hindered on-site field work. Usually, GCPs and check points should be spread out homogeneously, but the steep terrain and lush vegetation did not permit their even distribution. Then, based on terrain features and geomorphology, and considering adaptability, operability and rapidity, the plan for establishing and measuring the GCPs and check points was as follows (Fig. 5):

(1) 16 GCPs were established outside of the slope area (white disks in Fig. 5). According to the results of the engineering survey carried out in Aug. 2014 (Fig. 2), 16 feature points were established on the area of exposed bedrock around the slope. These points had unchanging positions and could be clearly distinguished on the photos acquired from the UAV. They were selected carefully in order to be used in SfM bundle adjustment image processing (Javernick et al. 2014; Lucieer et al. 2014; Turner et al. 2015). It should be noted that the 3D coordinates of the 16 GCPs came from the large-scale topographic map of Aug. 2014 and were used for image processing twice, using data from May 10 and Sept. 13, 2015.

(2) 3 GCPs and 4 check points were established on the middle to lower part of the slope (triangles in Fig. 5). Relatively gradual slopes and two terraces existed on this part, where humans could walk easily. Thus, 7 equally distributed feature points were selected in the field. Their 3D coordinates were measured with real-time kinematic (RTK) differential Global Positioning System (DGPS) techniques at the same time that images were acquired on May 10 and Sept. 13, 2015. All 7 points were used for accuracy assessment, and 3 of the points (white triangles in Fig. 5) were also used for SfM bundle adjustment.

(3) 3 GCPs and 2 check points were established on the upper part of the slope (pentagons in Fig. 5). Considering that the steep slopes of this part hindered on-site direct measurement, non-prism total station measurement techniques were used. Therefore, it was ensured that all points could be clearly distinguished in both the view from above seen in the UAV-based photos and the horizontal view seen from the total station, and that they could reflect strong and steady signals to the total station. 5 feature points which located at clear outcropped bedrock and big rock debris were selected carefully, and they were measured on May 10 and Sept. 13, 2015, respectively. Moreover, in order to ensure the measurement accuracy using non-prism total stations, two check points and one GCP which were measured by RTK DGPS and were located on the upper terrace of the slope (Figs. 2 3, 4 and 5) were used to compose the georeferenced network. Similarly, all 5 points were used for accuracy assessment, and 3 points (white pentagons in Fig. 5) were also used for SfM bundle adjustment.

Overall, a total of 28 GCPs were identified. Twenty-two GCPs were used for SfM bundle adjustment in the UAV-based image processing, and they fully covered the area inside and outside of the Qinglingou Slope. At the same time, all 28 points (including 6 independent check points) were used for accuracy assessment. On the other hand, only 7 points had to be measured by RTK DGPS, and 5 points had to be measured using a non-prism total station at the site.

Image-processing

The Pix4Dmapper software was chosen to process the photos (Strecha et al. 2012; Mesas-Carrascosa et al. 2015). This software can convert a large number of images into georeferenced 2D DSMs, digital orthophotos and 3D models using automatic aerial triangulation and bundle block adjustment. Therefore, the image processing was still photogrammetric (Strecha et al. 2012; Colomina and Molina 2014), but there was a difference relative to the conventional process in Pix4Dmapper: the

interior orientation, that is the camera calibration, was automated. Thus, a high-accuracy position orientation system (POS) such as an inertial measurement unit combined with a differential global positioning system (IMU/DGPS) was no longer needed on the UAV (although a DGPS was still needed). Accordingly, some camera parameters, including pixel size, focal length, etc. no longer had to be entered manually.

Automatic aerial triangulation consists of determining the individual orientation of each stereo model of a photogrammetric block. One of the most commonly used methods involves bundle adjustment, more specifically, the SfM-based bundle adjustment (Westoby et al. 2012; Mesas-Carrascosa et al. 2015). First, features were extracted from individual photos that could be matched to their corresponding features in other photos. All the matched points were then used to establish the relative locations of the sensors during the flight and to simultaneously calculate the sensor parameters of each photo. Next, the estimated 3D positions of all points that had been measured from photographs were entered into a ground control coordinate system. The use of GCPs often significantly increases the accuracy of the results of SfM bundle adjustment, so 22 GCPs (Fig. 5) were used in the two phases of image processing of the Qinglingou Slope. Finally, dense point clouds could be produced by using multi-view stereo matching (Strecha et al. 2012; Mesas-Carrascosa et al. 2015). Based on these point clouds, two DSMs and digital orthophotos were produced.

Slope deformation identification and measurement

Based on the two orthophotos and the DSMs, the slope deformation between May 10, 2015 with Sept. 13, 2015 could be analyzed. Of course, high-precision registration was an important prerequisite (Martha et al. 2010; Immerzeel et al. 2014; Turner et al. 2015), and just as mentioned above, 22 GCPs were used to rectify the orthophotos and DSMs to the unified coordinate system during the image processing. This procedure was actually a co-registration process between the two results in both the horizontal (i.e., X and Y) and the vertical (i.e., Z) directions, and the accuracy could be assessed from the quantified spatial errors. In addition, to prepare the two DSMs for terrain change detection, it was necessary to check their registration accuracy in the vertical direction, because any differences in the height were the most important component of misalignment and should not be ignored (Martha et al. 2010; Turner et al. 2015). In this study, a simplified co-registration accuracy assessment was carried out by computing the vertical elevation offset of four stable areas on the two DSMs (Lucieer et al. 2014). The four areas were located outside of the slope and had unchanged elevations. They included a patch of concrete in front of a house in the north, the asphalt pavement of S312 in the southwest, and two outcropping rock masses in the southeast and northeast.

Then, change detection and image correlation methods could be applied to the two orthophotos or DSMs (Lucieer et al. 2014; Turner et al. 2015). For the Qinglingou Slope, field investigation showed it was generally stable, and only some local deformation was observed. Thus, a simple and quick method, i.e., calculating the differences between the two DSMs, was used to identify and measure these local deformations. The basic principle was easy to understand; as long as deformation had occurred, there would be changes in the DSMs. In other words, the slope deformation would be reflected by changes in the DSMs.

In view of this, the differences in the two DSMs was calculated to detect all changes in the slope surface. Then, the changes as a result of slope deformation (such as the collapse of soil and/or rock) must be identified from the set of all DSM changes, which may include changes caused by vegetation, human activity, etc. Finally, using all the DSM changes that were caused by slope deformation, the spatial characteristics of slope movement could be concluded. Moreover, volume changes could be quantitatively calculated.

In the whole process, digital orthophotos were also necessary for visually interpreting, identifying and validating all changes in the DSMs.

Results

Accuracy of DSMs and orthophotos

Two orthophotos and DSMs showing the Qinglingou Slope are displayed in Fig. 6. In addition, 93 photos were used for image processing on May 10, 2015. Some blurred photos that were caused by turbulence and wind on Sept. 13, 2015 were omitted, so only 85 photos were used in the second image processing. Thus, the area covered on Sept. 13, 2015 was less than the first on May 10, 2015. For ease of comparison and analysis, the GSD estimated from the two data sets were resampled to 5 cm/pixel from the original resolution of 4.6 cm/pixel.

16 GCPs that are located outside of the slope, 6 GCPs and 6 check points that are located inside of the slope (Fig. 5) were used for accuracy assessment. The average, minimum, maximum, standard deviation, and root-mean-square error (RMSE) values were calculated. A summary of the results is presented in Table 1. It can be seen that the errors were less than 10 cm for both the GCPs and the check points.

At the same time, by computing the vertical elevation offset of the four stable areas shown on the two DSMs, the results of the co-registration accuracy assessment in the vertical direction were obtained. These results are presented in Table 2. The absolute elevation error between the two DSMs for the four stable areas was 0.147 m with a standard deviation of 0.152 m.

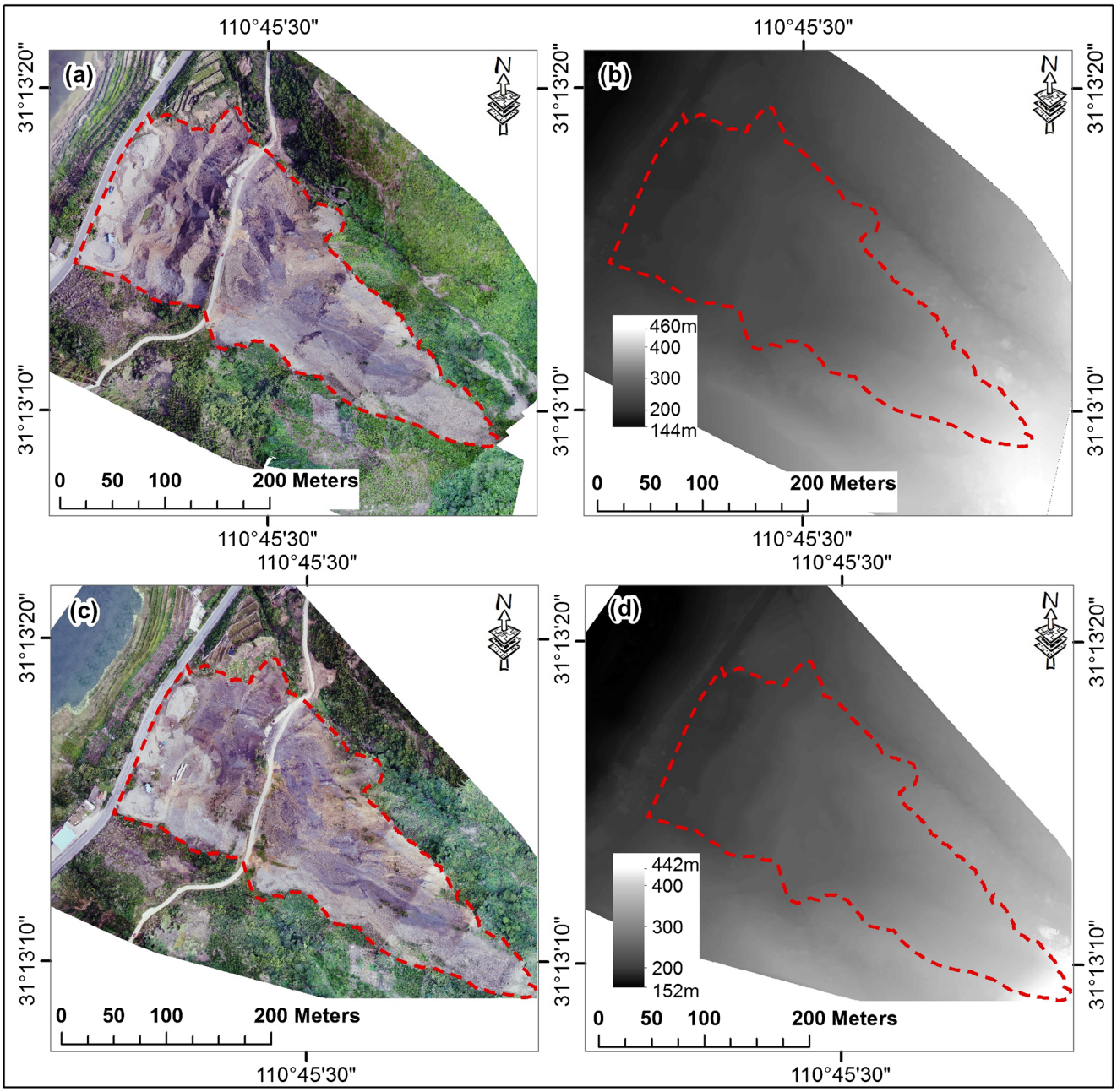

Fig. 6 Two digital orthophotos and DSMs showing the Qinglingou Slope: **a** digital orthophoto from May 10, 2015; **b** DSM from May 10, 2015; **c** digital orthophoto from Sept. 13, 2015; and **d** DSM from Sept. 13, 2015

DSM change

The DSM changes are presented in Fig. 7. On the whole, the zones of obvious change (> 15 cm) shown in the DSMs are mainly distributed outside of the slope boundary, and most areas inside of the slope showed no obvious change. This result indicated that the Qinglingou Slope was stable on the whole. Eight representative zones of DSM change were then delineated (A1-D2 in Fig. 7). These zones were caused by poor image quality and processing, vegetation change, human behavior, and slope deformation.

Slope deformation

Based on detailed analysis of D1 and D2 in Fig. 7 and in orthophotos, the signs of slope deformation could be identified. Based on these signs, six zones were delineated (Fig. 8). That is, from May 10, 2015 to Sept. 13, 2015, six local deformations occurred on the Qinglingou Slope.

Accordingly, to quantify the volume of each slope deformation, the per-pixel DSM difference was multiplied by the area of a single pixel (0.0025 m^2 for the 0.05 m GSD of the DSMs) and then summed within each deformation zone

Table 1 Summary of spatial errors of the two orthophotos and DSMs

Location	Type	Accuracy assessment index	May 10, 2015			Sept. 13, 2015		
			X Error (± m)	Y Error (± m)	Z Error (± m)	X Error (± m)	Y Error (± m)	Z Error (± m)
Outside of Slope Area	16 GCPs	Average	-0.013	0.018	-0.017	-0.056	0.004	0.014
		Minimum	-0.069	-0.071	-0.085	-0.109	-0.099	-0.109
		Maximum	0.063	0.077	0.091	0.105	0.092	0.106
		Stand. dev.	0.055	0.064	0.080	0.079	0.086	0.097
		RMSE	0.055	0.065	0.079	0.094	0.083	0.094
Inside of Slope Area	6 GCPs	Average	-0.025	0.003	-0.018	-0.070	0.031	-0.006
		Minimum	-0.060	-0.081	-0.087	-0.170	-0.074	-0.108
		Maximum	0.053	0.072	0.090	-0.004	0.122	0.113
		Stand. dev.	0.049	0.067	0.084	0.069	0.071	0.096
		RMSE	0.051	0.062	0.078	0.094	0.071	0.088
	6 Check points	Average	-0.021	0.023	-0.029	-0.025	-0.052	-0.027
		Minimum	-0.088	-0.081	-0.093	-0.168	-0.153	-0.169
		Maximum	0.066	0.074	0.094	0.117	0.038	0.096
		Stand. dev.	0.059	0.069	0.091	0.105	0.080	0.103
		RMSE	0.058	0.067	0.088	0.099	0.089	0.098

(Martha et al. 2010; Turner et al. 2015). The results are presented in Table 3.

Field validation

Figure 9 shows the six deformation zones on the Qinglingou Slope based on a field survey in September 2015, which was consistent with the results (Fig. 8). Obviously, D1 and D2 were easily observed, even by field surveys using ground-based cameras, because the two deformations occurred on the relatively flat areas where humans could walk easily. On the other hand, it was very difficult to observe D3 - D6 directly on the slope, because these deformations occurred in inaccessible steep areas. In fact, the photos of D3 - D6 were taken from the opposite mountain with a telephoto lens.

Discussion

Using a predetermined flight plan and autonomous flight, a UAV equipped with a camera could quickly collect photographs that covered the whole slope. The method has the particular advantages of high adaptability and flexibility, as well as low cost and risk (Fig. 3). During the first flight, the preliminary flight plan design and on-site verification were very important, especially because the height in the flight plan should change with the slope topography, usually keeping a relatively constant altitude difference; 100 m was a good choice in this study (Fig. 4). The successful flight plan could then be reused subsequently. Weather conditions could affect the image quality; there were more blurred photos on the second flight because of turbulence and wind, so the flight and image acquisition should be done on sunny days with no or light winds, but shadows should be avoided.

It was vital to establish GCPs and check points that would be visible during the flight to improve and assess the absolute geolocation accuracy. In general, these feature points should be placed homogeneously over the area of interest. For a moving slope or landslide, placing all points on stable locations located outside the slide mass was the best choice (Colomina and Molina 2014). However, for the Qinglingou Slope, the steep terrain and lush vegetation did not permit the use of this strategy. Thus, a detailed network of GCPs and check points was established and measured (Fig. 5): 16 GCPs located outside the slope area were selected from topographic maps and the UAV-based photos, and

Table 2 Assessment of the relative elevation accuracy of the two DSMs

Number of pixels within the four stable areas	Area (m^2)	Average	Minimum	Maximum	Stand. dev.	RMSE
226,138	565	0.057	-0.182	0.203	0.152	0.147

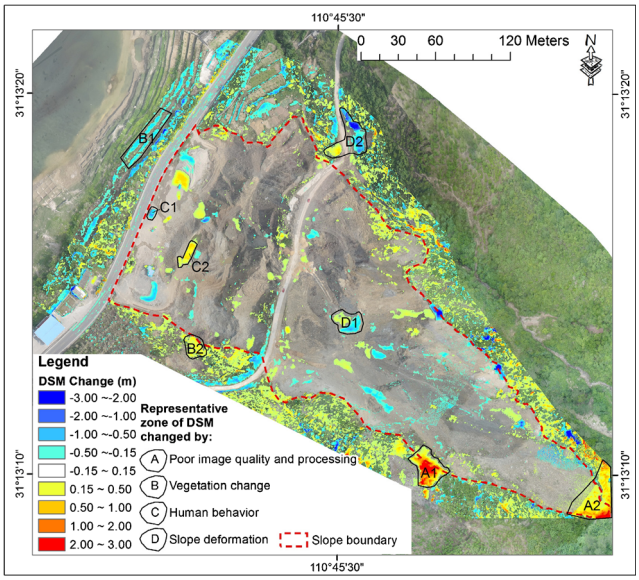

Fig. 7 Representative zones and DSM change on the Qinglingou Slope between May 10, 2015 and Sept. 13, 2015. The base map is a digital orthophoto from May 10, 2015

their 3D coordinates came from the large-scale topographic map of Aug. 2014, so the 16 GCPs were actually virtual in that neither setting nor measurement was needed on site. These GCPs could not only be used for image processing to improve the overall accuracy, but also avoided the difficulties of working in areas covered by lush vegetation. 3 GCPs and 4 check points were established on the relatively flat areas where humans could walk easily and measured using RTK DGPS, which is quick and accurate. Another 3 GCPs and 2 check points were identified remotely on the steep areas where humans could not walk and measured using a non-prism total station, which avoided the need to work on steep slopes and ensured the accuracy of these points.

According to the absolute position accuracy of the pairs of DSMs and orthophotos (Table 1), it can be seen that 1) the errors were less than 10 cm for both the GCPs and the check points, although the check points had larger errors than those of the GCPs; 2) compared with the accuracy of the 16 GCPs outside of the slope area, better results were obtained for the 6 GCPs inside of the slope area, which meant that more accurate 3D coordinates were obtained by using measuring instruments on site at the same time as the two flights than could be extracted from the earlier topographic map; 3) the errors associated with the second flight of Sept. 13, 2015 were larger than those of the first on May 10, 2015, which might be an indication of the influence of turbulence and wind on the second flight (Colomina and Molina 2014). In addition, compared with the adequate planar accuracy, the vertical accuracy was slightly poorer. In short, given the requirement to avoid the risk of working on steep slopes or those covered by lush vegetation, the plan for establishing and measuring GCPs and check points described above could still ensure satisfactory DSMs and orthophotos with good accuracy, and it was rapid, efficient and reliable to implement.

At the same time, the co-registration accuracy assessment of the two DSMs was an important precondition for change detection because of the importance of the differences in height (vertical Z direction). Therefore, a simplified co-registration accuracy assessment was carried out by computing the vertical elevation offset of four stable areas on the two DSMs. The results showed the absolute elevation errors between the two DSMs for the four stable areas was 0.147 m with a standard deviation of 0.152 m (Table 2). Co-registration accuracy assessment could ensure the validity of DSM change analysis, while poor vertical accuracy would inevitably lead to the errors in quantifying the deformation. Furthermore, the above co-registration accuracy assessment method would be too simple if accurate quantification (e.g., the volume change of slope deformation) was the key, in which case detailed accuracy assessment using robust statistical methods would be crucial (Prosdocimi et al. 2015).

By visually comparing the eight representative zones of DSM change (A1-D2 in Fig. 7) on the two orthophotos (Table 4), four reasons for the observed changes between the DSMs were identified as follows.

(1) Poor image quality and processing. Image blur, noise, overexposure, underexposure, distortion, low overlap between images, or images with homogeneous visual content such as dense vegetation or water, as well as other factors, could all lead to processing errors. In images A1 and A2 in Table 4, obvious image blur can be observed. Therefore, this type of DSM change represented false changes and usually occurred at the edges of the orthophotos.
(2) Vegetation change. Vegetation growth and decline, crop planting and harvesting, and even the motion of branches in the wind cause changes in the three-dimensional configuration of vegetation. Therefore, the DSM in vegetation-covered areas was inaccurate and unusable. B1 and B2 in Table 4 show crop harvesting and vegetation growth, respectively. This type of DSM change also represented false changes that could occur anywhere with vegetation cover.
(3) Human behavior. Human activities, such as artificial excavation to obtain rock and soil, etc. could change the earth's surface directly. They could also lead to slope deformation indirectly, so detailed inspection was necessary. For example, the car shown in C1 or the culvert pipes shown in C2 (Table 4) could lead to DSM changes. Obviously, this type of change also represented false and unrelated changes

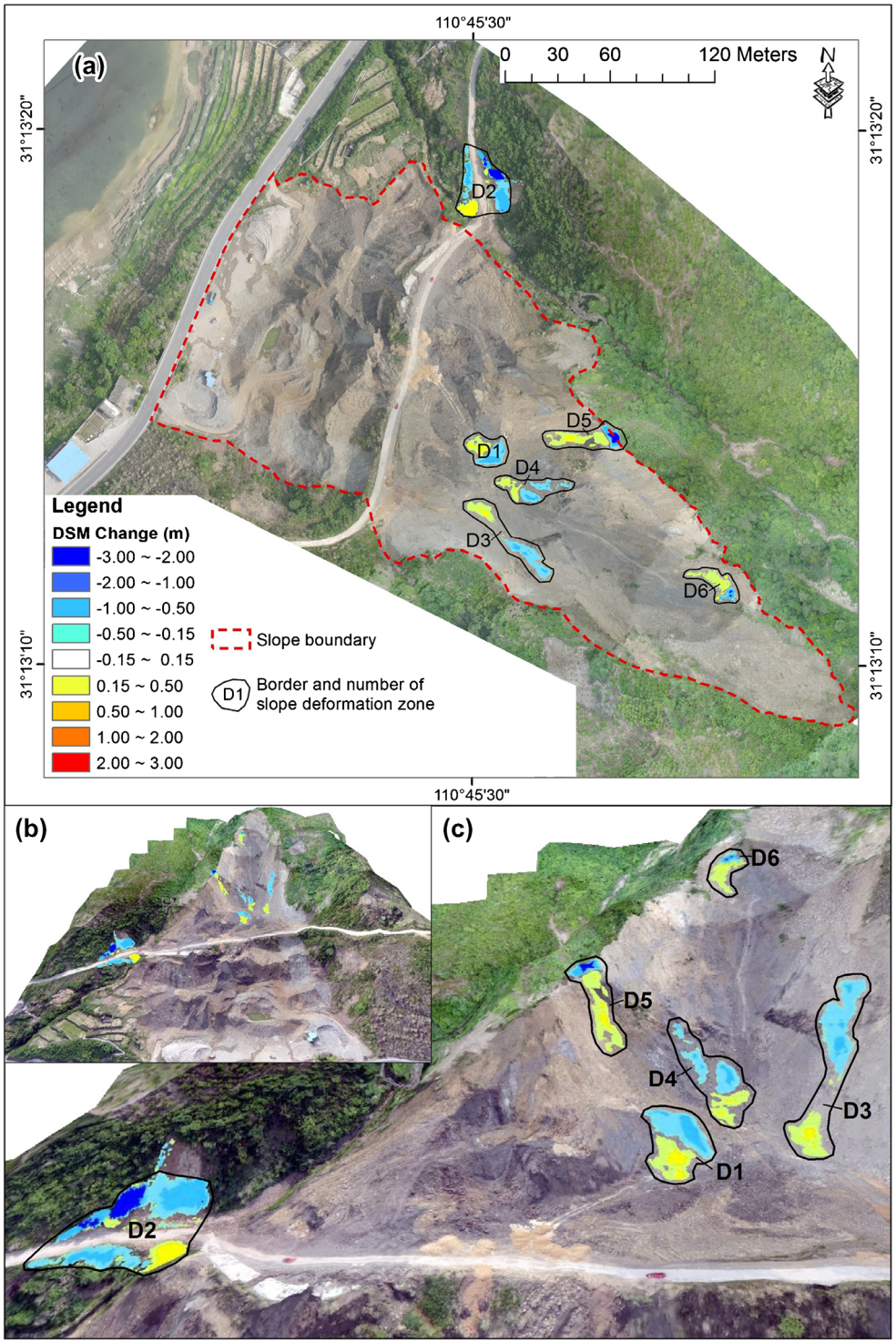

Fig. 8 Six deformation zones within the Qinglingou Slope occurring between May 10, 2015 and Sept. 13, 2015: (**a**) the base map is a digital orthophoto from May 10, 2015, (**b**) long-range view of deformation zones based on a 3D model from May 10, 2015, (**c**) close-range view of deformation zones based on a 3D model from May 10, 2015

that usually occurred on flat areas with convenient transportation.

(4) Slope deformation. As mentioned above, slope deformation was the movement of rock or/and soil, which definitely change the DSM. D1 and D2 in Table 4 show slope deformation, and the DSM changes associated with them are our primary concern.

Based on detailed analysis of D1 and D2 in Table 4, the DSM change characteristics that could be used for identifying slope deformation include:

(1) Vegetation-free areas as shown in the orthophotos were the main target zones. In other words, if slope

Table 3 Volume changes associated with six deformation zones on the Qinglingou Slope

Slope deformation zone	Loss (m^3)	Accumulation (m^3)	Difference (m^3)
D1	159	145	14
D2	252	223	29
D3	171	152	19
D4	122	109	13
D5	168	150	18
D6	77	69	8
Sum	949	848	101

deformation occurred in vegetation covered areas, the method of change detection using DSMs was inapplicable.

(2) Patches that covered a certain area and had uniform characteristics (whether increase or decrease) in terms of DSM change should be given more attention. When slope deformation occurs, a certain amount of material slides, collapses or flows downward, leading to a decrease in the DSM; the moving materials would subsequently stop and accumulate on gentler slopes, leading to an increase in the DSM.

(3) Composite patches with the following characteristics of DSM change were the areas of greatest concern. DSM decreased in the upper part of slope, and increased in the lower part. As in D1 and D2, they showed a combination of slope deformation, which included both material loss (where the DSM decreased) and accumulation (where the DSM increased) under natural conditions. It should be noted that the composite patches often showed some differences when slope deformation occurred in areas of human activities. For example, in D2 in Table 4, a collapse occurred on the slope that was located above the highway, leading to a large material loss. However, below the highway, only a small part of the material could be found. Obviously, the main accumulation that covered the highway was removed from the area due to human activity.

According to the above characteristics of slope deformation, six local deformations on the Qinglingou Slope were delineated. One of them (D2 in Fig. 8) lay on the village-level highway which traverses the middle part of the slope. The others (D1, D3, D4, D5, and D6 in Fig. 8) lay on the upper portion, i.e., the steepest part of the Qinglingou Slope. In addition, the six local deformation zones had similar topographical features, i.e., the soil or/and rock was located on steep areas. Regions of convex terrain were especially prone to slide, and the slide mass always accumulated below the slide, usually on flat or concave terrain, so that composite patches of DSM change (similar to those shown in D1 and D2 in Table 4) were formed.

Moreover, the volume change results showed that the accumulation was always less than the loss for each deformation zone (Table 3). This result might be due to a variety of reasons,

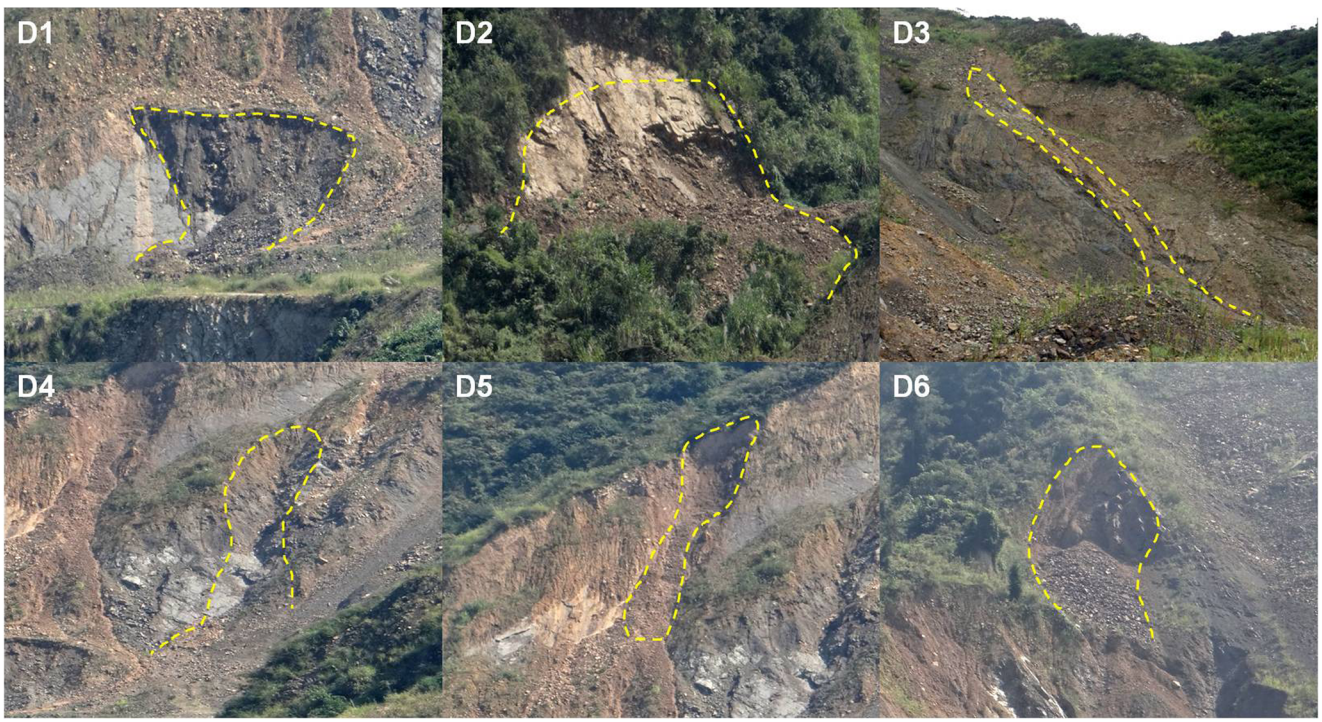

Fig. 9 Field observations of six deformation zones on the Qinglingou Slope in September of 2015

Table 4 Eight representative zones of DSM change

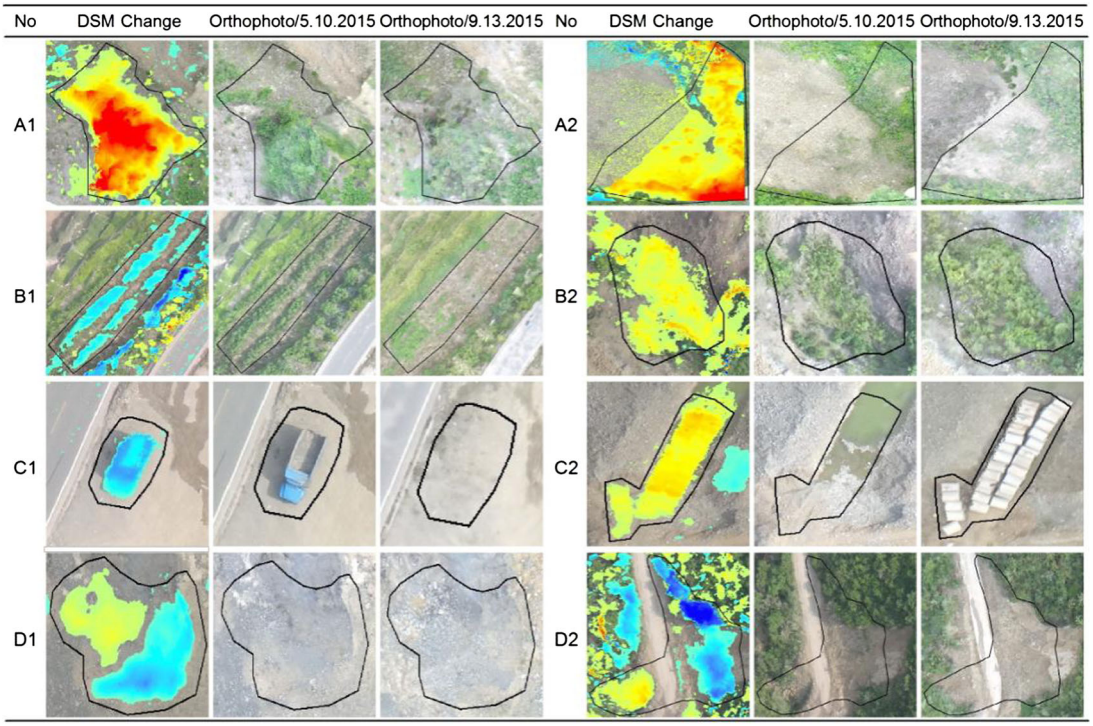

e.g., the loss of material by means of erosion by rain, human excavation work, etc. Moreover, unquantifiable situations could cause inaccurate results. For example, at D2, the lost volume that lay on the outer side of the highway could not be calculated because of vegetation change (see D2 in Table 4 and Fig. 8). At the same time, the part that originally covered the highway and then was cleared out of the area by humans could not be included in the calculation, so there was an apparent error and a big difference between the volume loss and accumulation. Furthermore, in this study, local slope movement characteristics and the vertical altitude error would also lead to inaccuracies in volume calculations, as explained in Fig. 10. First, the zone of loss, which was the original location

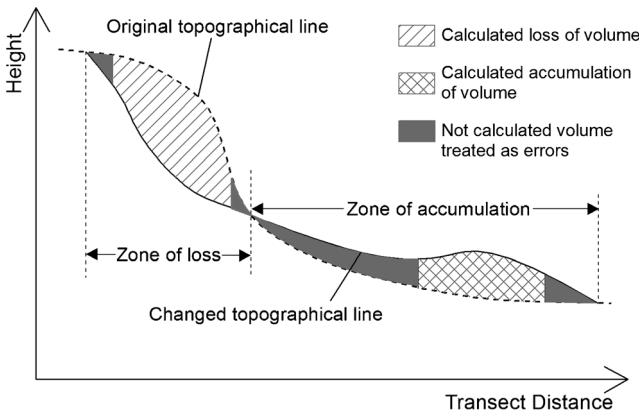

Fig. 10 Explanation of volume errors as the result of local slope movement characteristics and vertical altitude error

of the slide material, mainly lay on steep and convex terrain and thus had a relatively smaller planar area; on the other hand, the zone of accumulation usually had a greater length and also a greater planar area. Thus, under natural conditions in which the volume of loss is equal to the volume of accumulation, the average altitude difference (change of DSM) of the loss zone must be greater than that of the accumulation zone. Then, when calculating the volume change by considering a fixed altitude error (15 cm in the Qinglingou Slope), there must be some error in the estimated volume for both the loss and accumulation zones, but more volume of the accumulation zone was missed than in the zone of loss (gray part in Fig. 10). This difference explains why each volume of accumulation was less than the volume of loss in Table 3. Fundamentally, reducing the altitude error was the most important way to improve the accuracy of volume calculations.

Change detection and image correlation can usually be used for the analysis of slope or landslide deformation. Given that only local deformation was observed on the Qinglingou Slope, a simple and quick method that involved calculating and analyzing the changes between two DSMs and then identifying and quantifying slope deformation was used. The results showed that the method was effective, and it identified the spatial distribution and features of slope deformation and also provided the definite time interval of deformation. So, if UAV-based remote sensing methods were used to regularly monitor the Qinglingou Slope and analyze the temporal development of deformation, the detailed spatiotemporal

patterns and laws of deformation could be understood and guidance in controlling the slope deformation could be provided. However, it is worth noting that the method was mainly applied to slope or landslide areas that are vegetation-free and largely stationary.

Conclusions and recommendations

With the construction of Three Gorges Project and the impoundment of the Three Gorges Reservoir, many flat lowlands were inundated. Accordingly, a large number of steep mountainous slopes were formed because of extensive construction along the river banks, so the control of deformation within these steep mountainous slopes has become an important aspect of geo-hazards risk management in the Three Gorges Reservoir. Monitoring is considered to be the most effective means of mitigating and preventing geo-hazards, but it is challenging to carry out on steep mountainous slopes because the terrain and geomorphologic conditions of these slopes, for example their steep gradients and lush vegetation, greatly increase the risk and difficulties of field work.

In this paper, a UAV-based remote sensing system was used on the Qinglingou Slope, which is located at the head area of Three Gorges Reservoir. Based on two flights and image acquisition efforts, a complete UAV-based remote sensing method for monitoring and analyzing steep mountainous slopes was developed. The conclusions were as follows.

(1) The activity of the slope was limited to six localized and confined zones; that is, the slope as a whole was stable, which was consistent with the field investigation results.
(2) A UAV with a camera could quickly collect photographs of the slope surface and had the advantages of high adaptability and flexibility, as well as low cost and risk. Therefore, the UAV could make up for the deficiencies of traditional manual monitoring methods, which are hard to implement on steep mountainous slopes.
(3) Pix4Dmapper could convert a large number of images into 2D DSMs and digital orthophotos, which was the basis of our slope deformation analysis. Using GCPs could greatly increase the accuracy of the results, but a detailed plan for establishing and measuring GCPs and check points needed to be carefully designed according to the local conditions on steep mountainous slopes. The latest geological and topographic maps are valuable for setting these feature points. RTK DGPS techniques were suitable for measuring GCPs and check points on the relatively flat areas where humans could walk easily, while non-prism total station techniques might be the best choice for measuring points on the steep areas where humans could not walk.
(4) For vegetation-free slopes that are generally not moving, a simple and quick method that involved calculating and analyzing the change between two DSMs and then identifying and quantifying slope deformation was applicable. The process includes calculating the DSM changes, identifying reasons for the observed changes, identifying and delineating deformation zones, summarizing their characteristics and calculating volume changes.
(5) Four reasons which led to changes in the DSM included poor image quality and processing, vegetation change, human activity and slope deformation. Three signs of DSM change characteristics that could be used for identifying slope deformation, which are universal, were also identified.

In a word, a rapid, safe, effective and complete UAV-based remote sensing method was established that included on-site image acquisition, the establishment and measurement of GCPs and check points, image processing, and slope deformation identification and quantification. In addition, this method was a valuable reference for monitoring a large number of steep mountainous slopes in the Three Gorges Reservoir of China, as well as other places.

At the same time, some recommendations were developed, including:

(1) Improving the image processing accuracy, including the absolute geolocation accuracy, registration accuracy, etc. is a vital precondition whenever the surface deformation of slopes must be accurately quantified, as in volume measurements.
(2) For slopes or landslides that are moving over large areas, change detection and image correlation methods could be used on multi-temporal orthophotos or DSMs. In that case, more detailed deformation information, such as the surface movement vector field, might be obtained.

Acknowledgements This work was supported by the National Natural Science Foundation of China (41302260/D0215), the Open Research Fund of the Key Laboratory of Disaster Prevention and Mitigation of Hubei Province (2016KJZ16), the Open Research Fund of the Hubei Key Laboratory of Intelligent Vision Based Monitoring for Hydroelectric Engineering (2016KLA02), and in part by the Hubei Science and Technology Support Program (2015 BCE070, 2015 BCE038) and the Innovation Groups Project of the Natural Science Foundation of Hubei Province (2015CFA025).

References

Booth AM, Lamb MP, Avouac JP, Delacourt C (2013) Landslide velocity, thickness, and rheology from remote sensing: la Clapière landslide, France. Geophys Res Lett 40:4299–4304

Bürkle A, Segor F, Kollmann M (2011) Towards autonomous micro UAV swarms. J Intell Robot Syst 61:339–353. doi:10.1007/s10846-010-9492-x

Colomina I, Molina P (2014) Unmanned aerial systems for photogrammetry and remote sensing: a review. ISPRS J Photogramm 92:79–97. doi:10.1016/j.isprsjprs.2014.02.013

Dewitte O, Jasselette JC, Cornet Y, Van Den Eeckhaut M, Collignon A, Poesen J, Demoulin A (2008) Tracking landslide displacements by multi-temporal DTMs: a combined aerial stereophotogrammetric and LIDAR approach in western Belgium. Eng Geol 99:11–22

Harwin S, Lucieer A (2012) Assessing the accuracy of georeferenced point clouds produced via multi-view stereopsis from unmanned aerial vehicle (UAV) imagery. Remote Sens-Basel 4:1573–1599. doi:10.3390/rs4061573

Huang H, Yi W, Lu S, Yi Q, Zhang G (2014a) Use of monitoring data to interpret active landslide movements and hydrological triggers in three gorges reservoir. J Perform Constr Facil 30: C4014005

Huang H, Yi W, Yi Q, Lu S (2014b) Real-time Monitoring And Data Analysis Of An Active Landslide In Three Gorges Reservoir. In Engineering Geology for Society and Territory - Volume 2 SE - 253, G. Lollino et al., Ed., pp. 1433–1436 m, Springer International Publishing.

Huang B, Zheng W, Yu Z, Liu G (2015) A successful case of emergency landslide response - the Sept. 2, 2014a, Shanshucao landslide, three gorges reservoir. China Geoenvironmental Disasters 2. doi:10.1186/s40677-015-0026-5

Immerzeel WW, Kraaijenbrink PDA, Shea JM, Shrestha AB, Pellicciotti F, Bierkens MFP, Jong SMD (2014) High-resolution monitoring of Himalayan glacier dynamics using unmanned aerial vehicles. Remote Sens Environ 150:93–103

Javernick L, Brasington J, Caruso B (2014) Modeling the topography of shallow braided rivers using structure-from-motion photogrammetry. Geomorphology 213:166–182. doi:10.1016/j.geomorph.2014.01.006

Jian W, Xu Q, Yang H, Wang F (2014) Mechanism and failure process of Qianjiangping landslide in the three gorges reservoir, China. Environ Earth Sci 72:2999–3013

Joyce KE, Belliss SE, Samsonov SV, McNeill SJ, Glassey PJ (2009) A review of the status of satellite remote sensing and image processing techniques for mapping natural hazards and disasters. Prog Phys Geogr 33:183–207. doi:10.1177/0309133309339563

Kasperski J, Delacourt C, Allemand P, Potherat P, Jaud M, Varrel E (2010) Application of a terrestrial laser scanner (TLS) to the study of the Séchilienne landslide (Isère, France). Remote Sens-Basel 2: 2785–2802. doi:10.3390/rs122785

Lucieer A, Jong SMD, Turner D (2014) Mapping landslide displacements using structure from motion (SfM) and image correlation of multi-temporal UAV photography. Prog Phys Geogr 38:97–116. doi:10.1177/0309133313515293

Malet JP, Maquaire O, Calais E (2002) The use of global positioning system techniques for the continuous monitoring of landslides: application to the super-Sauze earthflow (Alpes-de-haute-Provence, France). Geomorphology 43:33–54

Martha TR, Kerle N, Jetten V, van Westen CJ, Kumar KV (2010) Landslide volumetric analysis using cartosat-1-derived dems. IEEE Geosci Remote Sens Lett 7:582–586

Mesas-Carrascosa F, Torres-Sánchez J, Clavero-Rumbao I, García-Ferrer A, Peña J, Borra-Serrano I, López-Granados F (2015) Assessing optimal flight parameters for generating accurate multispectral Orthomosaicks by UAV to support site-specific crop management. Remote Sens-Basel 7:12793–12814. doi:10.3390/rs71012793

Niethammer U, Rothmund S, Joswig M, Bogaard T, Malet JP (2009) UAV-based remote sensing of the slow-moving landslide Super-Sauze. Landslide Processes: 69–74

Niethammer U, Rothmund S, James MR, Travelletti J, Joswig M (2010) UAV-based remote sensing of landslides. Int Arch Photogramm Remote Sens Spat Inf Sci 38:496–501

Niethammer U, Rothmund S, Schwaderer U, Zeman J, Joswig M (2011) Open source image-processing tools for low-cost UAV-based landslide investigations. Int Arch Photogramm Remote Sens Spat Inf Sci 38:C22. doi:10.5194/isprsarchives-xxxviii-1-c22-161-2011

Niethammer U, James MR, Rothmund S, Travelletti J, Joswig M (2012) UAV-based remote sensing of the Super-Sauze landslide: Evaluation and results. Eng Geol 128:2–11. doi:10.1016/j.enggeo.2011.03.012

Niu R, Wu X, Yao D, Peng L, Ai L, Peng J (2014) Susceptibility assessment of landslides triggered by the Lushan earthquake, April 20, 2013, China. IEEE J-Stars 7:3979–3992. doi:10.1109/JSTARS.2014.2308553

Prosdocimi M, Calligaro S, Sofia G, Fontana GD, Tarolli P (2015) Bank erosion in agricultural drainage networks: new challenges from structure-from-motion photogrammetry for post-event analysis. Earth Surf Process Landf 40:1891–1906. doi:10.1002/esp.3767

Rawat MS, Joshi V, Rawat BS, Kumar K (2011) Landslide movement monitoring using GPS technology: A case study of Bakthang landslide, Gangtok, East Sikkim, India. J Dev Agric Econ 3:194–200

Santamaria E, Pastor E, Barrado C, Prats X, Royo P, Perez M (2012) Flight plan specification and management for unmanned aircraft systems. J Intell Robot Syst 67:155–181. doi:10.1007/s10846-011-9648-3

Strecha C, Küng O, Fua P (2012) Automatic mapping from ultra-light uav imagery. Paper presented at the EuroCOW 2012, Barcelona, Spain, 8-10 February 2012

Tahar KN (2012) A new approach on slope data acquisition using unmanned aerial vehicle. Intern J Res Rev Appl Sci 13:780–785

Tofani V, Segoni S, Agostini A, Catani F, Casagli N (2013) Technical note: use of remote sensing for landslide studies in Europe. Nat Hazards Earth Syst Sci 13:299–309. doi:10.5194/nhess-13-299-2013

Turner D, Lucieer A, de Jong SM (2015) Time series analysis of landslide dynamics using an unmanned aerial vehicle (UAV). Remote Sens-Basel 7:1736–1757. doi:10.3390/rs70201736

Westoby MJ, Brasington J, Glasser NF, Hambrey MJ, Reynolds JM (2012) 'Structure-from-Motion' photogrammetry: a low-cost, effective tool for geoscience applications. Geomorphology 179:300–314. doi:10.1016/j.geomorph.2012.08.021

Yin Y (1998) Research on geologic hazards of relocation construction at the Three Gorges Reservoir, the Yangtze River. Chinese J Geol Hazard Cont 9:59–66 (in Chinese)